A Reverse-Engineering Method for Powertrain Parameters Characterization Applied to a P2 Plug-In Hybrid Electric Vehicle with Automatic Transmission

2020-37-0021

A reverse-engineering method for powertrain parameters characterization applied to a P2 Plug-In Hybrid Electric Vehicle with Automatic Transmission

Giuseppe Di Pierro, Enrico Galvagno, Gianluca Mari, Federico Millo, and Mauro Velardocchia

Politecnico di Torino

Alessandro Perazzo

FEV Group GmbH

Abstract

Over the next decade, CO2 legislation will be more demanding and the automotive industry has seen in vehicle electrification a possible solution. This has led to an increasing need for advanced powertrain systems and systematic model-based control approaches, along with additional complexity. This represents a serious challenge for all the OEMs. This paper describes a novel reverse engineering methodology developed to estimate relevant powertrain data required for fuel consumption-oriented hybrid electric vehicle (HEV) modelling. The estimated quantities include high-voltage battery internal resistance, electric motor and transmission efficiency, gearshift thresholds, torque converter performance diagrams, engine fuel consumption map and front/rear hydraulic brake torque distribution. This activity provides a list of dedicated experimental tests, to be carried out on road or on a chassis dynamometer, aiming at powertrain characterization thanks to a suitable post-processing algorithm. In this regard, the methodology was applied on a P2 Diesel Plug-in HEV equipped with a 9-speed AT. Voltage and current sensors are used to measure the electrical power exchanged between battery and electric motor; a torque sensor on the propeller shaft measures the total torque coming out from the automatic transmission. The hydraulic pressures in the four brake calipers are measured and CAN data is logged. The results of the testing campaign are then presented and discussed. Functional models of powertrain subsystems are introduced and their parameters estimated using least square method. The good match between models and experimental data proved that the proposed methodology, if properly adapted to the specific layout, is a suitable tool for powertrain parameter estimation.

Introduction

The global automotive market currently fits one billion cars, mostly powered by an Internal Combustion Engine (ICE) [1]. As a countermeasure to face the continuously growing number of vehicles and the impact that the transportation sector has on the environment, worldwide government have introduced regulations with more stringent emission standards, more demanding in terms of fuel consumption and CO2 emission reduction [2]. As for the passenger-car major markets, it was estimated that technological development has to be pushed further in order to annually improve fuel economy by 3–6% [3]. As a consequence, Original Equipment Manufacturers (OEMs) have innovated their technology portfolio over the last decades, resulting in significantly cleaner and efficient cars [4]. In this framework, powertrain electrification offers the potential for a substantial emission reduction; the electrification process does not only include Battery Electric Vehicles (BEVs), but also vehicles powered by an ICE such as mild hybrids (MHEVs) [5], full hybrids (HEVs) [6–9], and plug-in hybrids (PHEVs). Electrified vehicles are clearly a part of the future of transportation [10]. Even though the IC engine has always been a part of the system, industry and consumers request is changing [11]. In this context, the interest towards Plug-in Hybrid Electric Vehicles (PHEVs) is growing [4], since these vehicle offer both the benefits of a BEV and of a full HEV, by enabling the ICE operation during the Charge Sustaining (CS) mode [12].

On the other side, newly developed HEV powertrains features a High Voltage (HV) network whose voltage ranges between 100 and 600 V. These powertrains generally combine one or more powerful EMs with a downsized engine [13,14], enabling the need of additional components for extra safety features, additional cooling systems for the HV battery and the power electronics, and DC-DC converters to feed the low voltage (LV) side. As a consequence, the complexity of today's powertrains has increased [15,16]. Moreover, considering that all these subsystems work together to monitor and control various aspects of the vehicle, the picture becomes even more complicated [17]. As far as the vehicle development is concerned, it is crucial to understand how subsystems are composed and in which way they mutually interact, in order to be able to explain their behavior and physically model them by means of maps and physical equations. To this extent, HEV testing can be a first step for creating database and improving technical knowledge, as multiple systems and different energy sources have come into play. Therefore, HEV development would clearly benefits from a detailed and specific reverse-engineering methodology [17], with the aim of fully characterize the different devices installed on these powertrains, such as ICE, EM, Transmission, Battery and other subsystems.

In this regard, the proposed research activity presents a reverse-engineering method applicable to new-generation HEV powertrains, in order to characterize the main systems. It is worth mentioning that the presented activity is intended to be carried out at vehicle level, avoiding the need to perform a more expensive vehicle teardown. More in details, the case study of this paper is a Euro 6d-temp P2 Diesel Plug-In Hybrid Electric Vehicle (PHEV) already available on the market, equipped with a 9-speed Automatic Transmission (AT). The investigated powertrain can be regarded as the state of the art in terms of Diesel engine technology and hybrid electric powertrain; it was instrumented both on the thermal, electrical, hydraulic and mechanical side, in strategic locations that will be presented in detail over the next sections. Afterwards, the vehicle was tested on a chassis dynamometer under a specific test procedure which involves a limited number of tests, with the aim of exploring different operating points and extract as much data as possible. The implementation of a

dedicated and sustainable testing methodology has been already introduced and developed in previous publications [18,19]. Particularly, in this paper the authors focused on characterizing the ICE efficiency and fuel consumption, the EM efficiency, the torque converter maps and the HV battery main parameters, i.e. the open circuit voltage and the internal resistance. A dedicated investigation was performed to assess the transmission efficiency and to identify the thresholds that trigger gear shifting. Finally, the braking system behavior was investigated thanks to a dedicated instrumentation and test campaign. It is important to say that, for each analysis, the testing maneuver is firstly introduced by showing the time history of the relevant quantities, then, look-up tables or functional models for the powertrain subsystems are introduced, after that, the unknown parameters/maps are identified through a suitable signal processing algorithm and, finally, experimental validation is shown.

This paper is structured as follows. The first section outlines the main vehicle and powertrain characteristics, together with the instrumentation setup and the test protocol designed for the proposed methodology. Later in the *Results and Discussion* section the outcome of the experimental campaign and the parameter identification process are shown and discussed. Lastly, the research activity is summarized along with the main findings and conclusions.

Methodology

Tested Vehicle

The vehicle under investigation is a P2 Diesel Plug-In Hybrid Electric Vehicle (PHEV) available on the market. Other than a conventional 1950 cc Diesel engine, this vehicle features a 90kW/440 Nm Permanent Magnet Synchronous (PMSM) electric motor, mounted in P2 position, i.e. downstream the ICE by means of an auxiliary clutch (K0). In this case, the hybrid powertrain is coupled with a 9-speed automatic transmission and a torque converter that transfer the torque to the rear wheels, according to a Rear-Wheel-Drive configuration. Thanks to the powerful electric motor and the 13.5 kWh Li-Ion nickel-manganese-cobalt-oxide (NMC) HV battery, the PHEV is capable of driving in all-electric mode at a top speed of 130 km/h. The main vehicle characteristics are listed in

Table 1, while a schematic of the powertrain is shown in Figure 1.

.

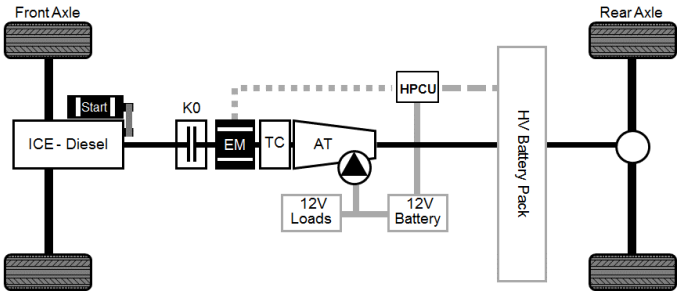

Figure 1: Powertrain schematic and main components

Table 1:Vehicle and powertrain main specifications.

Engine (ICE)			
Engine Type	In-line 4 cyl. Turbo Diesel		
Displacement	1950 cc		
Max Power / Max Torque	143kW @3800rpm / 400Nm @1600-2800 rpm		
Compression Ratio	15.5:1		
Transmission			
Type	9 –AT w/ Torque Converter		
Speed Ratios	I 5.36 II 3.25 III 2.26	IV 1.64 V 1.22 VI 1.00	VII 0.87 VIII 0.72 IX 0.61
Reverse – Final Drive	- 4.93	2.65	
Vehicle			
Curb Weight	2060 kg		
Configuration	Rear Wheel Drive (RWD)		
Electric Motor (EM)			
Type	PM Synchronous motor		
Max Power / Max Torque	90 kW / 440 Nm @1750rpm		
Max Speed	6000 rpm		
High Voltage Battery			
Type	Lithium- NMC		
Rated Voltage	365V		
Capacity	13.5kWh / 37 Ah		
Cooling System	Water Cooled		

Depending on the driver's demand, the four listed operating modes can be chosen:

- **Hybrid Mode**: it is the default setting; all functions, such as electric driving, boost and energy recovery, are available according to the driving situation and route profile
- **Electric mode**: electric driving by means of the main traction motor, for example in the city center. The accelerator triggers the pressure point at which the combustion engine is started
- **E-Save**: electric motor propels the vehicle in combination with ICE, but it will be ensured that constant SOC is maintained regardless, in order to allow electric driving mode later
- **Charge**: the battery is constantly charged while driving via the ICE load, the electric motor does not give contribution to vehicle propulsion

Experimental Setup

The main part of the experimental test campaign was carried out on an All-Wheel Drive (AWD) Chassis Dyno. The vehicle test bench is made up by two rollers of 1219.2 mm of diameter and 1150 kg of actual mass. The chassis dyno allows a maximum driving speed of 250 km/h and a maximum combined power (front and rear) of 230 kW. The permitted vehicle mass ranges from 800 to 3650 kg, with a force measurement accuracy less than 2 Nm and a speed accuracy of ±0.08 km/h. The upper part of Figure 2 depicts a 3D render of the adopted roller bench and its main components. The electric machine (pos 2) is the core of the bench since it acts as a motor/generator to reproduce the road conditions via the rollers (pos 3); to cool down the electric machine, a fan is placed next to it (pos 1). In position 4 the speed sensor is placed, used for the closed loop control. Moreover, the shaft bearings (pos 5), the roller shaft (pos 7), the emergency brake (pos 8) and the roller centering device (pos 9) are shown. More in details, the load measurement group is marked in pos 6, attached to the machine case. The torque applied to the measurement device is transmitted to the force sensor via the lever, as depicted in the schematic in the bottom part of Figure 2. The sensor output is a voltage that is converted into a corresponding torque value thanks to a periodical calibration performed during the maintenance work.

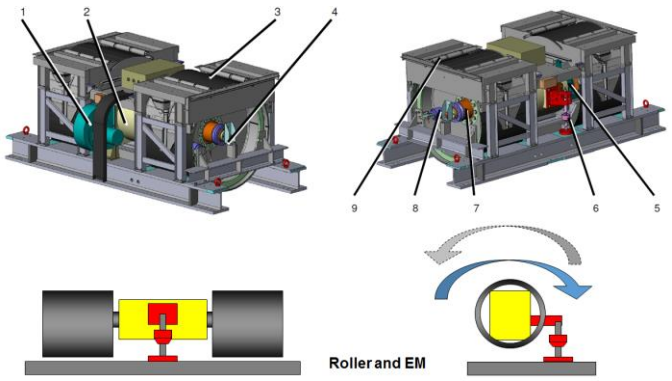

Figure 2: Vehicle Chassis Dynamometer render (top) and force measurement sensor schematic (bottom) [20]

Before entering the testing environment, the vehicle and its main sub-system were carefully instrumented in order to perform the desired powertrain characterization. The following sections will introduce the different type of instrumentation involved in the presented activity, such as the powertrain, the transmission output shaft and the braking system.

Powertrain Instrumentation

This section deals with the instrumentation of the powertrain devices that are mainly involved in propelling the vehicle. In this regard, Figure 3 shows a more detailed schematic of the vehicle layout: the Hybrid Power Control Unit (HPCU) is a unique block with the HV inverter that is responsible for delivering the energy between the HV battery and the electric motor (EM). Within the HPCU a DC/DC converter is placed; it has the aim of feeding the auxiliary 12V battery and so all the 12V loads placed onboard. For example, this vehicle fits a common 12V starter, and an electrical oil pump for gearbox lubrication. On the electrical side, the authors decide to instrument the HV battery DC input/output (I/O) in order to detect its energetic balance; the HPCU High Voltage side and the DC/DC Low Voltage side. Finally, the 12V battery output was instrumented to investigate the energy flow used for auxiliary purposes.

The electrical measurements were performed with the ISAscale® IVT-S high precision current and voltage measurements system. The shunt sensor have to be placed in series with the electrical load, on the positive side. The shunts current range is of ±1000 A and the voltage range of ±600 V [21]. Later, a 16-bit analog-to-digital converter is adopted to transform the shunt signals into a digital current signal. The communication is based on a CAN bus interface, via a CSM®'s AD MiniModules (ADMM). As already mentioned, this vehicle features only an AC PM Synchronous motor, which the authors did not instrument because of the complexity of the system and the consequent heavy and costly effort required in data acquisition and processing. Therefore, the EM characterization was carried out using the electrical energy measured on the DC side and some data available on the CAN bus. To this extent, it is worth to mention that some of the variables used for the investigation were acquired using both the On Board Diagnostic (OBD [22]) and the vehicle CAN-bus protocol; for example, engine speed and torque as well as EM speed and torque were measured via CAN.

Another important aspect is the vehicle thermal management, hence temperatures in key locations were measured by means of Type 'K' (Nickel Chromium/Nickel Aluminum) thermocouples, working in a range from -40°C to +1100°C [23]. As depicted in Figure 3 by a star marker, the ICE temperature was recorder by measuring the input and output of the coolant circuit; with the aim of distinguish between the cold-start phase and the normal running mode. Additionally, temperature sensors were placed on the secondary cooling circuit, used to cool down of the HV system; thus the coolant temperature at the inlet and outlet of the HV battery, and its surface temperature were acquired. In this regard, coolant temperature at both inlet and outlet of the power electronic box (HPCU) and the EM were measured, in order to add another degree of freedom to the powertrain characterization. Analogic signals coming from the thermocouples were collected and converted into digital signals by means of a CSM®'s Thermo MiniModules (THMM).

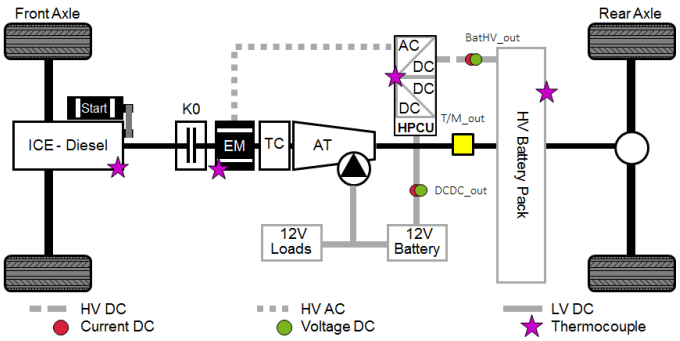

Figure 3: Powertrain layout with instrumentation details

Transmission Output Shaft Instrumentation

In order to measure the propeller shaft torque, a strain gauge sensor with a telemetry system has been installed on the vehicle, as depicted in Figure 3 by a yellow-square marker. This system is typically used when there is the need to measure the torque in a precise location without modifying the layout of the transmission system. For this study the torque has been measured at the transmission output, installing the sensor in a safe position from road and temperature

shocks due to the exhaust pipeline. Figure 4 illustrates the strain gauge sensor application on the propeller shaft. A strain gauge sensor (2) is a device useful to measure deformations of a body subjected to mechanical stresses. It is characterized by a very fine wire grid stuck on a plastic support. The strain gauge sensor is used by gluing it on the surface of the body whose deformations have to be measured. The strain gauge wire follows the deformations of the surface to which it is glued, lengthening and shortening together with it. These dimensional variations cause a variation in the electrical resistance of the wire, therefore, by measuring these variations using the appropriate equipment, it is possible to trace the extent of the deformation that caused them. Deformations, and so voltage variations, are then linked to the torque by means of appropriate equations, explained later. After the application, the strain gauge sensor is connected to a transmitter (4) with a Wheatstone bridge configuration. For measuring the transmission output torque, a full-bridge configuration has been chosen with the aim of maximizing the amplification of the output signal and compensate effects like thermal expansion and bending deformation. The transmitter is connected to a coil (5), whose number of windings depend on the shaft diameter; and it uses induction to communicate with an antenna. The aim of the antenna is to power the transmitter (and so the strain gauge sensor) and exchange the output data coming from the sensor. The sensor output is a voltage variation sent to the telemetry system, which is later transformed into a torque value.

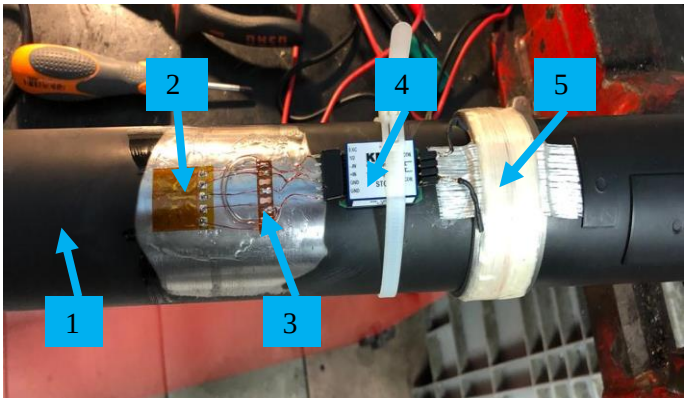

Figure 4: Strain gauge sensor installation on a transmission output shaft: 1-Transmission shaft, 2-Strain gauge sensor, 3-Base for welding, 4-Transmitter, and 5-Coil.

The Wheatstone bridge equations are hereafter reported:

$$\frac{V_{AB}}{V_s} = \frac{K_{SG}}{4}(\varepsilon_1 - \varepsilon_2 + \varepsilon_3 - \varepsilon_4) \quad (1)$$

$$\varepsilon_1 = \varepsilon_3 = \varepsilon \quad (2)$$

$$\varepsilon_2 = \varepsilon_4 = -\varepsilon \quad (3)$$

$$\frac{V_{AB}}{V_s} = K_{SG}\varepsilon \quad (4)$$

Where V_{AB} is the output voltage of the Wheatstone bridge, V_s is the supply voltage of the Wheatstone bridge, K_{SG} is the strain gauge factor, ε_i is the normal strain of the i-th grid of the strain gauge (oriented at 45° with respect to the shaft axis). According to Mohr's circle theory, in the pure torsional stress state, the maximum value of the main stress σ_z is equal to the maximum tangential stress, as reported in the following equations.

$$\sigma_1 = -\sigma_2 = \tau_{max}\ ;\ \sigma_3 = 0 \quad (5)$$

Then, the normal strain measured by the strain gauge can be computed:

$$\varepsilon = \frac{1}{E}\sigma_1 - \frac{\nu}{E}\sigma_2 - \frac{\nu}{E}\sigma_3 = \frac{1}{E}\tau_{max} + \frac{\nu}{E}\tau_{max} = \frac{1+\nu}{E}\cdot\tau_{max} \quad (6)$$

Where: $\sigma_1, \sigma_2, \sigma_3$ are the principal stresses, ε is the normal strain, E is the Young modulus, ν is the Poisson modulus and τ_{max} is the maximum tangential stress. The Wheatstone bridge equation can be rewritten as follows:

$$\frac{V_{AB}}{V_s} = K_{SG}\cdot\varepsilon = K_{SG}\cdot\frac{1+\nu}{E}\cdot\tau_{max} \quad (7)$$

where τ_{max} , in the case of torsion of a circular hollow shaft, can be computed as a function of the applied torque T, which is the real objective of the measure:

$$\tau_{max} = \frac{T}{I_p}\cdot R_e \qquad \text{where} \qquad I_p = \frac{\pi(R_e^4 - R_i^4)}{2} \quad (8)$$

I_p is the polar area moment of inertia of the shaft cross section, R_e and R_i are the shaft external and internal radii. Substituting eq. (8) in eq. (7) yields:

$$\frac{V_{AB}}{V_s} = K_{SG}\cdot\frac{1+\nu}{E}\cdot\frac{T}{I_p}\cdot R_e \quad (9)$$

To compute the output voltage of the telemetry system, the bridge output voltage must be multiplied by the gain K_{TEL} set on the telemetry, six gains from 250 to 8000 are selectable via a rotary switch.

$$V_{out,tel} = K_{TEL}\cdot V_{AB} = K_{TEL}\cdot V_s\cdot K_{SG}\cdot\frac{1+\nu}{E}\cdot\frac{T}{I_p}\cdot R_e \quad (10)$$

The gain K_{TEL} must be set properly in order to exploit all the voltage range $V_{out,tel,max} = 10V$ and have a more precise measurement, given that the number of bits of the analog to digital converter is fixed. It can be computed as follows:

$$K_{TEL} = \frac{V_{out,tel,max}\ E\ I_p}{V_s\ K_{SG}\ (1+\nu) R_e\ T_{max}} \quad (11)$$

Finally, the constant of proportionality K_{TOT} between shaft torque and telemetry output voltage is:

$$T_{out} = K_{TOT}\cdot V_{out,tel} = \frac{E\cdot I_p}{K_{TEL}\cdot V_s\cdot K_{SG}\cdot(1+\nu)\cdot R_e}\cdot V_{out,tel} \quad (12)$$

T_{out} is the shaft torque to be measured, K_{TOT} is the total gain of the measuring system and K_{TEL} is the telemetry gain. As a result, Table 2 summarize the values of K_{TOT} in relation to the K_{TEL} set. Moreover, in the table is possible to see the resolution and the torque that can be measured for each telemetry gain.

After the instrumentation and calibration phase, torque can be effectively measured; Figure 5 shows the comparison between the shaft power measured by the strain gauge sensor and the one measured by the test bench, scaled down by an estimated 98% final drive efficiency, in a sequence of acceleration and deceleration test.

Table 2: Measure resolution, total gain and torque range for each telemetry gain

K_{TEL}	Measure resolution [Nm]	K_{TOT} [Nm/V]	Torque range [Nm] (10 V)
250	4.3	**874.9**	± 8749
500	2.1	**437.4**	± 4374
1000	1.1	**218.7**	± 2187
2000	0.5	**109.4**	± 1094
4000	0.3	**54.7**	± 547
8000	0.3	**27.3**	± 273

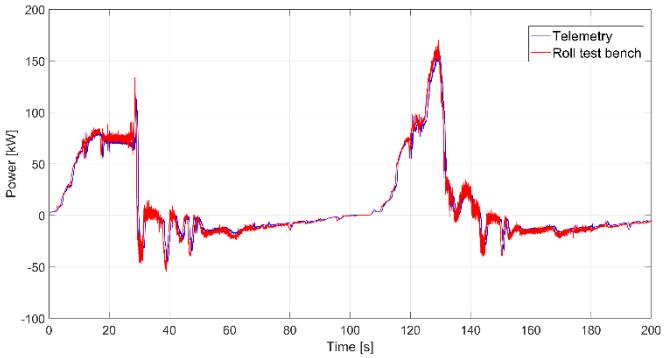

Figure 5: Power comparison between telemetry measurement and test bench measurement.

Vehicle Braking System Instrumentation

The analysis of the braking system aims at investigating two important aspects of the vehicle behavior: the brake blending between hydraulic and electric, and the vehicle dynamics during a deceleration. This analysis was carried out by means of four pressure sensors placed on the brake calipers, and one on a master cylinder chamber. In this regard, the authors adopted five commercially-available active pressure transducer, ideal for any automotive application, completely made of stainless steel (AISI 316 L). The SPA100 pressure sensors have a 0-100 bar range, with a linear characteristic output of 0 to 5V [24]. Figure 6 illustrates the schematic of the braking system and the instrumentation effort carried out on the four calipers and on one side of the master cylinder output line. It can be noticed that the braking system circuit has been replaced by a black-box in the figure since the only purpose is to give the reader an idea of the sensor location and not to deeply investigate the different circuit components and the way they work.

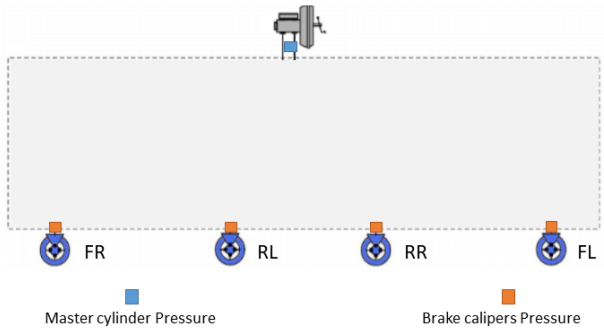

Figure 6: Schematic of braking system instrumentation

Test Protocol

As already mentioned, for powertrain characterization chassis-dyno testing was performed. To simulate the road resistance, the Road Load (RLs) coefficient were determined according to the WLTP regulations [25,26]: values are listed in Table 3.

Table 3. Vehicle Road Loads and Test Mass for WLTC

Variable	Unit	Value
Test Mass	Kg	2162
F0	N	171.5
F1	N/(km/h)	0.833
F2	N/(km/h)^2	0.0280

Once the chassis dyno is set, the vehicle can be placed on the test bench for the experimental campaign. In this regard, Table 4 illustrates in detail the different types of tests performed for vehicle characterization and their specific purpose. The *Ramp-Up* tests are carried out at constant and imposed chassis-dyno speed, depressing the accelerator pedal by steps, for different gears. *Constant Drive* test is again performed at constant speed but controlled by the driver as normal on-road driving. Also, this test investigates different engine/EM load and speed, varying the selected gear. Finally, both Acceleration and Deceleration maneuvers were carried out exploring different accelerator pedal positions or different deceleration rates via a suggested vehicle speed profile.

Table 4: Detailed test campaign for powertrain characterization

DYNO TEST	DESCRIPTION	SCOPE	MODE
Ramp-Up	Dyno steady speed, acc. pedal sweep, repeat for each gear	AT Efficiency EM Efficiency ICE Efficiency	Hybrid Electric Hybrid
Constant Drive	Steady speed	Battery Modeling	Hybrid
Acceleration	0 – 100 km/h, different acc. pedal	Gearshift Threshold Torque Converter	Hybrid
Deceleration	Different constant deceleration levels	Braking System Gearshift Threshold	Hybrid
Driving Cycle	WLTC	Overview Torque Converter	Hybrid

In the *Results and Discussion* section, an example of the test will be given along with the outcome of the specific test campaign. To sum up, all the tests were useful to gathered important data for powertrain characterization.

Results and Discussion

In this section, the results of the experimental campaign and the parameter identification process will be explained and discussed. More in details, for each characterized component, the authors will explain the testing maneuver specifications along with a time-based significant plot. Afterwards, the data analytical elaboration will be given, based on the equations found in literature that are used to describe the investigated phenomena. Finally, results will be shown against data collected during the experimental campaign.

Results of the identification process

For the sake of brevity, an example of the specific maneuver will be given for each aspect of the powertrain characterization. Afterwards, the experimental data are used to identify the parameters that best describe the investigated phenomena. To this extent, the methodology was applied to characterize the AT efficiency, the gearshift threshold maps, the torque converter performance diagrams, the efficiency of both the EM and the ICE, the HV battery circuit and, finally, the braking system behavior.

Transmission Efficiency

In order to compute the transmission efficiency, the output data coming from the dedicated tests (see Table 4) are used. Depending on the direction of the power flow through the transmission, transmission efficiency is calculated as follows:

$$\eta_t = \begin{cases} \frac{P_{AT,out}}{P_{AT,in}}, \ P_{AT,out} > 0 \ , \ Drive \\ \frac{P_{AT,in}}{P_{AT,out}}, \ P_{AT,out} < 0 \ , Coast \ / \ Regen \end{cases} \quad (13)$$

Where P is the mechanical power entering or exiting the transmission: $P_{AT,in}$ is the power evaluated on the motor side, while $P_{AT,out}$ is the power computed on the propeller shaft side. The first equation is related to the drive mode, in which the power flows from the powertrain to the wheels, while the second equation describes the coast or regeneration mode when the power flow goes from the wheels to the powertrain. For this type of analysis, it is necessary to reach stationary conditions. More in detail, the so-called *Ramp-Up* tests aim at reaching a combination of speed and load (torque), for each selected gear, as displayed in Figure 7.

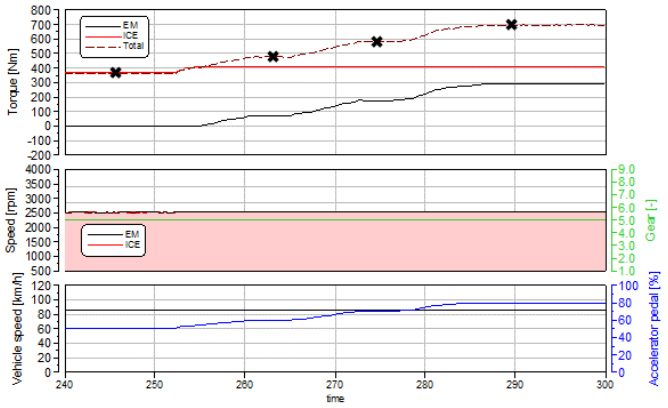

Figure 7: Powertrain torque (top), speed and gear (bottom) and vehicle speed with accelerator pedal position (bottom) during a Ramp-up test for transmission efficiency calculation

In this case, the picture above shows the recorded EM and ICE torque, as well as the total transmission input torque equal to the contribution of both the EM and the ICE. As reported in the second sub-plot, the gear selected is the 5th and the powertrain rotates at 2500 rpm, since the coupling clutch K0 is closed. Due to the high power request, the ICE is turned on and the EM works as a booster to assist during the maneuver. From the last plot, it can be seen that a constant speed of 85km/h is imposed by the rollers while the accelerator pedal is gradually depressed.

As shown by the experimental and simulated trends in [27], transmission efficiency has a strong dependency on input torque C_{IN}. A simple model implementation of this behavior is by using two parameters, i.e. the mesh efficiency η_m and the minimum input torque C_0 to have positive efficiency, as written in the following equation:

$$\eta_{AT} = \eta_m \cdot \left(1 - \frac{C_0}{C_{IN}}\right) \quad (14)$$

In order to estimate these two parameters (C_0 and η_m), an ordinary least squares analysis has been performed. The previous equation (14) has been transformed into the following matrix form:

$$AX = B \quad (15)$$

$$A = \begin{bmatrix} 1 & -\frac{1}{C_{IN_1}} \\ \vdots & \vdots \\ 1 & -\frac{1}{C_{IN_n}} \end{bmatrix}, B = \begin{bmatrix} \eta_{AT_1} \\ \vdots \\ \eta_{AT_n} \end{bmatrix}, \ X = \begin{bmatrix} \eta_m \\ C_0 \cdot \eta_m \end{bmatrix} \quad (16)$$

Where *n* represents the number of measures considered for the parameter estimation and the vector of the unknowns X includes the two model parameters we are looking for. The best fit solution is computed as follows:

$$X = A^{-1}B \quad (17)$$

where A^{-1} is the pseudoinverse of A.

Figure 8 shows the comparison between the analytical model (blue dash-dotted line) and the validation set of experimental data (orange dots) in Vth gear at 2500 rpm. In order to estimate the model

parameters, the previous analysis has been computed for few carefully chosen experimental points (estimation data set), indicated by the four cross markers in Figure 7 and 8, verifying that the speed and torque condition is constant and stable. By comparing the transmission efficiency obtained from the model with the experimental data a coefficient of determination R^2 of 0.95 has been found for the estimation data set.

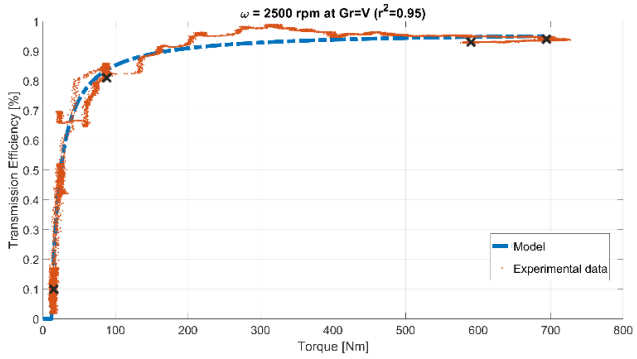

Figure 8: Transmission efficiency correlation between the model (blue line) and the experimental data (orange dots)

For the sake of completeness, this procedure should be applied for different operating points in terms of gears and speed, which will allow the user to create a complete transmission efficiency map, as a function of speed, torque and gear engaged under controlled temperature conditions.

Electric Motor Efficiency

In order to define the electric motor efficiency, the exploration of the whole EM working map is required. To do so, the same type of procedure previously explained for the transmission efficiency has been used, since the aim is to record the electric and mechanical energy during steady-state operation. In this regard, one can see from the top plot of Figure 7 how the EM torque is gradually increased by acting on the accelerator pedal position. After testing the PHEV over different driving condition as for speed and load, the recorded operating points in motor mode (EM torque>0) are plotted in the EM working map, as illustrated in Figure 9: the top black curve is the EM full-load curve in peak operation, while the orange dots represent the operating points.

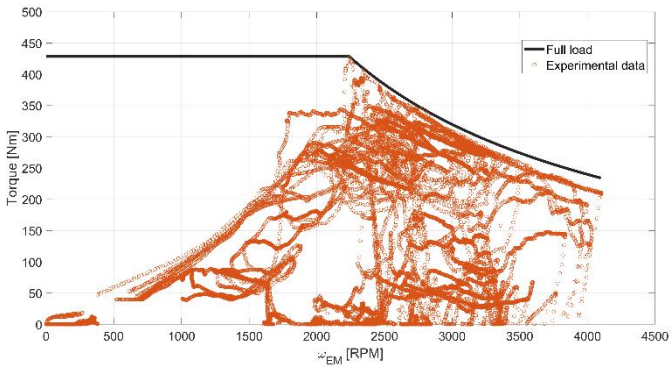

Figure 9. Electric motor working points in speed (x-axis) torque (y-axis) map and full-load curve

As previously illustrated for the transmission efficiency calculation, it is possible to define an analytical expression also for the EM efficiency. For this purpose, the *Willians Line Model* for an Electric Machine is adopted [28]. In this model, the input and output power are normalized by the geometrical parameters of the EM, such as the rotor radius r and its volume V_{rotor}, as reported in the following equation:

$$p_{me} = \frac{T_{EM}}{2 \cdot V_{rotor}} \qquad p_{ma} = \frac{I \cdot V}{V_{rotor}} \cdot \frac{2 \cdot \pi}{\omega} \qquad c_m = r \cdot \omega \tag{18}$$

According to this model assumption, the output torque is defined as:

$$T_{EM} = e\, T_a - T_{loss} \tag{19}$$

The p_{me} can be rewritten as:

$$p_{me} = \frac{e \cdot p_{ma}}{4 \cdot \pi} - \frac{r \cdot W_{loss}}{2 \cdot V_{rotor} \cdot\ c_m} \tag{20}$$

Where e is an internal efficiency and W_{loss} are the power losses. As already explained, an ordinary least squares analysis has been performed in order to find unknown variables such as e and W_{loss}

$$AX = B \tag{21}$$

$$A = \begin{bmatrix} p_{ma_1} & -\frac{1}{c_{m_1}} \\ \vdots & \vdots \\ p_{ma_n} & -\frac{1}{c_{m_n}} \end{bmatrix}, B = \begin{bmatrix} p_{me_1} \\ \vdots \\ p_{me_1} \end{bmatrix}, X = \begin{bmatrix} C_0 \\ C_1 \end{bmatrix} \tag{22}$$

$$X = A^{-1}B \tag{23}$$

Where

$$C_0 = \frac{e}{4 \cdot \pi} \quad , \quad C_1 = \frac{r \cdot W_{loss}}{2 \cdot V_{rotor}}. \tag{24}$$

To this extent, Figure 10 shows the output of the correlation between the model (blue surface) and the experimental data (orange dots). It can be seen that the *pme* has a linear dependence with the *pma* if the speed is constant.

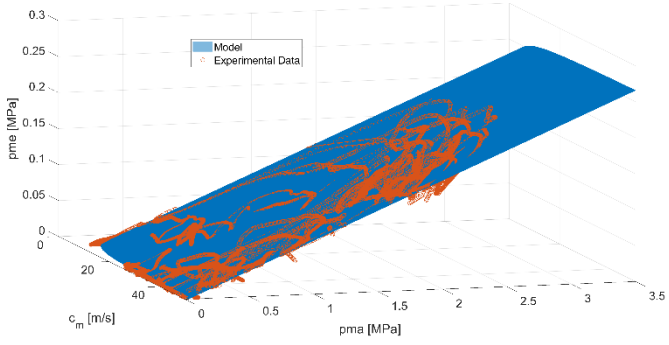

Figure 10. Pme correlation between model (blue) and experimental (orange) data, as a function of pma and cm

From the previous picture, it can be noticed that the model shows good agreement with the experimental data, resulting in an R^2 value of 0.85. This method can be used to identify the unknown parameters

e and W_{loss} necessary for the EM efficiency characterization, expressed as follows:

$$\eta_{EM} = \frac{\omega \cdot T_e}{I \cdot V} = \frac{\omega \cdot T_e}{e \cdot \omega \cdot T_e + W_{loss}} = 4\pi \cdot \frac{p_{me}}{p_{ma}} \qquad \textit{motor mode} \qquad (25)$$

The identified EM efficiency model is depicted in Figure 11 by means of iso-efficiency curves together with the experimental data used for parameter estimation. This figure shows a comparison between EM modelled efficiency (iso-curves) and experimental efficiency values (cross markers), obtained in points (Torque, ω) close to the stationary conditions.

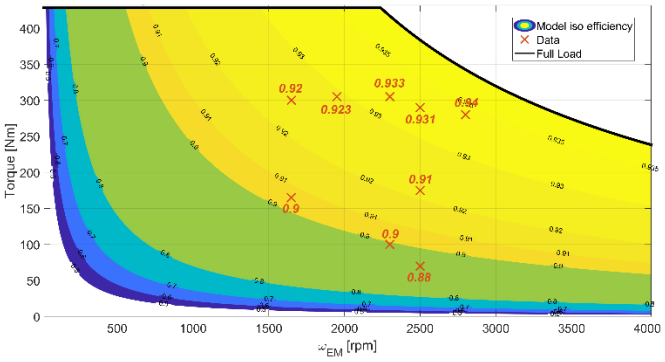

Figure 11 EM motor measured (cross) and modelled (contours) efficiency

In addition, it can be seen that the highest efficiency region is located in the central-right area of the EM working map, with a maximum level of 94%, where the majority of the working point displayed in Figure 9 are placed.

Internal Combustion Engine Efficiency

The IC Engine efficiency is normally assessed via detailed tests carried out on an engine test bench, which requires the ICE to be disassembled from the powertrain and set up on the dedicated bench. The idea is to run the engine in a series of stationary points in terms of rotational speed and load, the compute the brake torque generated and the amount of fuel consumed [29]. In this research activity, the aim is to gather a sufficient amount of data for powertrain characterization by vehicle testing, avoiding the need of tearing up the complete powertrain. For this reason, the output of the test previously described for the EM efficiency were used as well for the calculation of the brake specific fuel consumption. As a further example, Figure 12 shows data recorded during the *Ramp-Up* test on the chassis dyno, in order to explore steady operating points as for speed and load, i.e. torque (grey band). In this example the dyno is set to 100 km/h, while the driver performs a pedal acceleration sweep (bottom); meanwhile the EM supports the ICE in propelling the vehicle (top). This procedure is carried out for different gears, in order to explore different rotational speeds over the ICE working map.

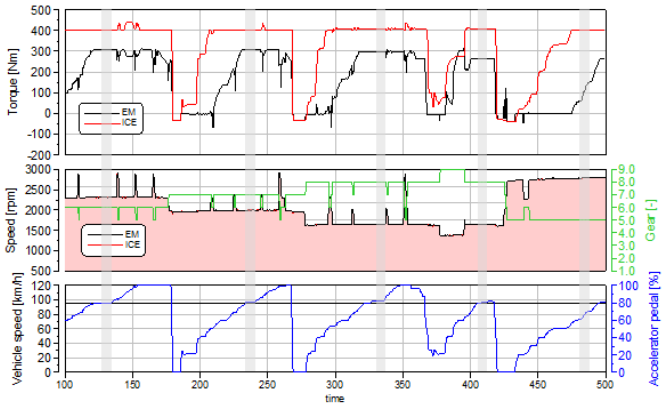

Figure 12: Powertrain torque (top), speed and gear (center) and vehicle speed with accelerator pedal position (bottom) during a Ramp-up test for BSFC

The working principles of the internal combustion engine implies that only a fraction of the fuel chemical energy is converted into mechanical energy at the crankshaft. The ICE efficiency can be calculated as follows [30]:

$$\eta_u = \frac{L_u}{m_b \cdot Q_{HV}} = \frac{P_u}{\dot{m}_b \cdot Q_{HV}} \qquad (26)$$

Where L_u and P_u are respectively the engine useful work and power, m_b and $\dot{m}_b$ are respectively the mass and flow rate of fuel burnt and Q_{HV} is the fuel lower heating value. Typically, literature introduces the brake specific fuel consumption (BSFC) as a parameter to express the efficiency of an ICE. The word "brake" refers to the dynamometer adopted to measure the engine torque and power.

In the experimental context here presented, the fuel mass flow rate $\dot{m}_b$ was acquired as a signal available on the CAN network, as well as the engine torque T_{ICE} and speed ω_{ICE} that are used to calculate the ICE mechanical power $P_u = T_{ICE} \cdot \omega_{ICE}$, which is delivered at the crankshaft. With these two quantities, it is possible to evaluate the BSFC as follows:

$$BSFC = \frac{\dot{m}_b}{P_u} \qquad (27)$$

The engine efficiency can be easily evaluated starting from the BSFC, as reported in the equation below:

$$\eta_u = \frac{1}{BSFC \cdot Q_{HV}} \qquad (28)$$

It was possible to calculate the BSFC in various operating points, by driving the vehicle at constant speed and load, acting on the accelerator pedal to control the engine torque to the wheel and acting on the gear engaged to control the ICE rotational speed. Finally, the engine working maps was computed as illustrated in Figure 13: the calculated BSFC [g/kWh] is plotted by means of iso-BSFC, i.e. iso-efficiency contours, as a function of engine speed [rpm] and load [bar], or Brake Mean Effective Pressure (BMEP). The data extracted from the experimental campaign are shown in white circles. It can be noticed that the engine high-efficiency region covers the central operating area and results in a BSFC of 207-215 g/kWh of BSFC.

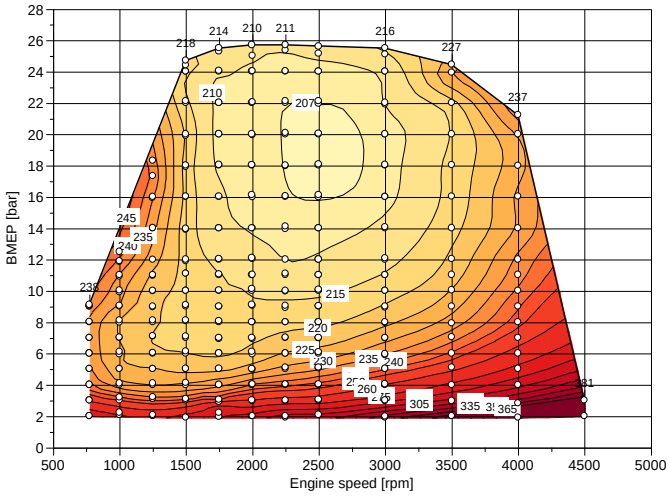

Figure 13: Engine BSFC map, function of speed [rpm] and BMEP [bar]

HV Battery Equivalent Model

Regarding vehicle simulation, the HV battery is often simulated as a simple equivalent model, as shown in the (a) plot of Figure 16. To do so, it is important to characterize two main parameter, such as the Open Circuit Voltage (OCV) and the internal resistance [31].

During the experimental campaign, a wide range of battery SOC, current and voltage was explored by performing two constant-speed test with the aim of respectively deplete and recharge the HV battery by driving. It is worth mentioning that the SOC variable used for the battery characterization is acquired by CAN data and it reflects the user displayed value. This means that the SOC variables is an indication of the actual energy capacity used by the battery, which is not equal to the nominal capacity for safety and durability reasons. Hence, the experimental and model signals will exploit a 0-100% artificial range, which reflects the battery net energy content. In this regard, Figure 14 shows the HV battery SOC and power traces (top) along the full-depletion test, together with the battery current and voltage (bottom). As one can notice, the battery is discharged until 13% of SOC at almost constant power of around 13 kW.

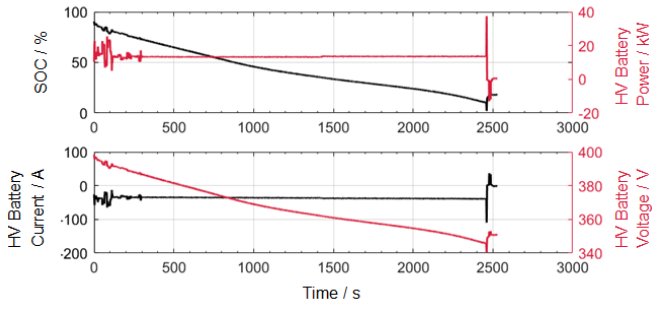

Figure 14. Full-depletion test recordings. SOC and Battery Power (top), Current and Voltage (bottom)

On the other side, a 50-km/h constant-speed test in Charge mode was carried out in order to characterize the HV battery during the charging phase. As it can be noticed from Figure 15, the vehicle is driven with constant engine load and power (top), while the battery energy content rises linearly from around 23% to 35%.

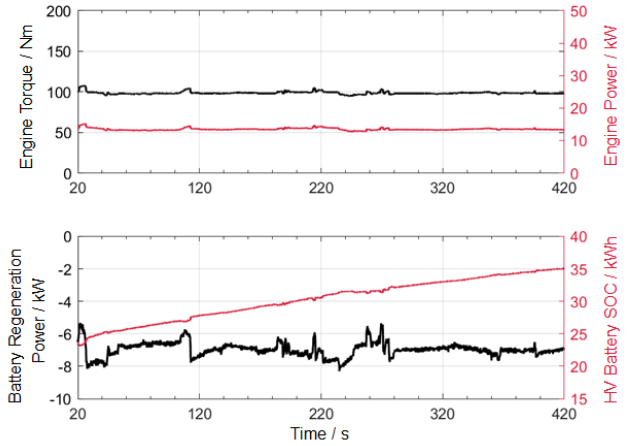

Figure 15: 50km/h charging drive test recordings. Engine torque and power (top), SOC and Battery Power (bottom)

As for the Lithium- NMC battery technology cell, the OCV and the internal resistance are functions of the cell SOC and the cell temperature. Therefore, this analysis uses data available in the scientific literature [32,33] as a starting point of the characterization process. Later, to account for the effects of the cell chemistry, the electrode material composition, the electrolyte ionic conductivity, and the fact that the model involves the complete battery pack rather than the single cell, the model parameters were experimentally characterized by achieving the same battery voltage output, which was measured during the aforementioned tests.

As illustrated by the model in Figure 16 and in the instrumentation section, the battery current and voltage are measured during the tests. The voltage across the battery load and the OCV are linked by the following equation:

$$\Delta V = (OCV - I \cdot \mathrm{R}_{Int}) \cdot nr_{cells} \qquad (29)$$

Where ΔV and I are measured, while the OCV and R_{Int} are initially taken from literature and nr_{cells} is the number of cells in series configuration. To this regard, in the (b) plot of Figure 16 the reader can find the output of the previous equation both for the measured output voltage (black line) and the first-tentative modelled voltage (blue line), during charging and discharging, using values found in literature for a Li-ion NMC battery. After this, the same equation has been rewritten with the adoption of some coefficient that will be later calibrated, as follows:

$$\Delta V_{sim} = (\alpha \cdot OCV - I \cdot \beta \cdot \mathrm{R}_{Int}) \cdot nr_{cells} \qquad (30)$$

Where ΔV_{sim} is the model voltage, while α and β are the two parameters used to calibrate the new resistance and OCV maps, either for the charging and discharging test. To this extent, a root mean square error (RMSE) minimization problem has been solved; which results in both OCV and internal resistance map variations, with an adjusted R^2 of around 0.995. The three maps shown in Figure 16 are respectively: $\beta_{ch} \cdot R_{int}$ (c), $\beta_{dch} \cdot R_{int}$ (d) and $\alpha \cdot OCV$ (e), where α has been chosen to be an average of the charging and discharging modelling. As one can notice from the curves, these values a Figure 16 are calculated at cell level to reflect the average data available in literature. As a result of the minimization process, the (f) plot of Figure 16 shows the new modelled output voltage (blue) and the

same measured voltage (black) during the charging and discharging test.

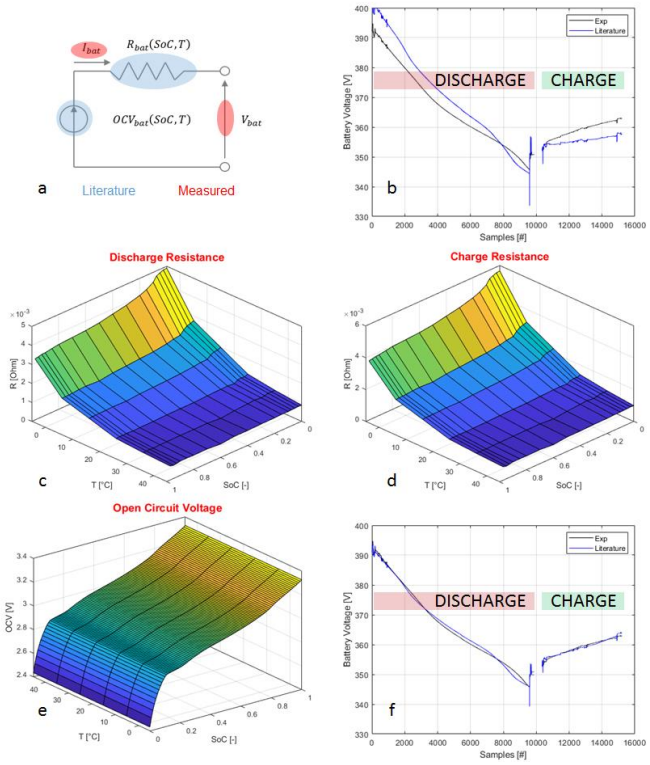

Figure 16: Battery equivalent Thevenin Model Characterization (a), raw voltage output (b), discharge (c) and charge (d) corrected resistances, corrected OCV (e) and optimized model voltage output (f).

Torque Converter Parametrization

The characterization of the torque converter (TC) is focused on the identification of the two performance maps: the capacity factor and the torque ratio as functions of the speed ratio. The torque converter is located between the EM and the automatic gearbox; it mainly operates during vehicle take-off, whenever the powertrain torque needs to be amplified or the torsional vibration damped [34]. To characterize the behavior of this device, the powertrain has to be tested under specific conditions that requires the lock-up clutch to be open. Therefore, data are acquired during a series of start-up maneuvers carried out on the chassis dyno. As depicted in Figure 17, the acceleration is very smooth, since the effect of the powertrain inertia has to be avoided when comparing the different torque in action, both on the input and the output side.

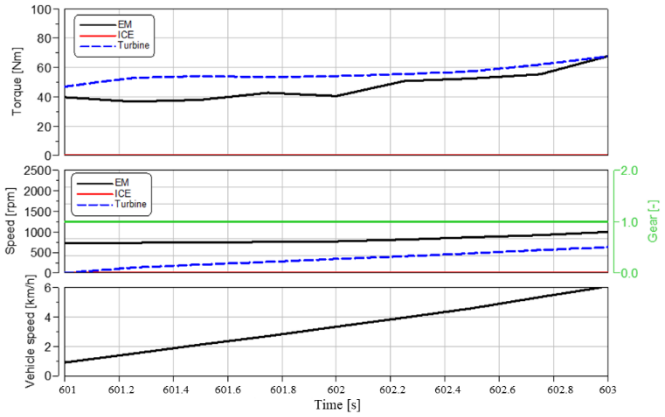

Figure 17: Torques (top), rotational speeds and gear (middle), vehicle speed (bottom) over a dedicated acceleration test

More in details, Figure 17 reports the main signals acquired, such as the torque converter pump, turbine and ICE speeds and vehicle speed. In the upper plot the pump, turbine and ICE torque are shown. It is worth to mention that, during a full-electric maneuver, the input (pump) torque is equal to the EM torque. TC pump rotational speed is always equal to the electric motor speed. Since the turbine side is difficult to access, this was not instrumented. Hence, this methodology calculates the output speed directly from the wheels speed, as follows:

$$\omega_p = \frac{Vel_{veh}}{R_w} \cdot \tau_{gb} \cdot \tau_{fd} \tag{31}$$

Where Vel_{veh} is the vehicle speed, R_w is the wheel rolling radius, τ_{gb} is the gearbox ratio and τ_{fd} is the final drive ratio. This procedure is not applicable during a gearshift event because the turbine speed can no longer be estimated from the actual gear ratio signal available on CAN. For the turbine torque estimation, the measurement provided by the telemetry system on the transmission output shaft T_{out} has been used. To calculate the turbine torque, the following equation was used (if the torque is positive):

$$T_t = \frac{T_{out}}{\tau_{gb}\eta_t} \tag{32}$$

Where T_t is the turbine torque, T_{out} is the strain-gauge measured torque, τ_{gb} is the gear ratio and η_t is the transmission efficiency, which was previously defined. To characterize the behavior of this device, it is necessary to distinguish two different working modes depending on the value of the speed ratio and torque ratio, defined as:

$$SR = \omega_t/\omega_p \tag{33}$$

$$TR = T_T/T_p \tag{34}$$

As explained in [35,36], the pump and turbine torques can be approximated with quadratic expressions. As for the torque converter working modes, it may operate in amplification mode (or converter mode) and in coupling mode [37,38].

$$\begin{cases} T_p = a_0{\omega_p}^2 + a_1\omega_p\omega_t + a_2{\omega_t}^2 \\ T_t = a_3{\omega_p}^2 + a_4\omega_p\omega_t + a_5{\omega_t}^2 \end{cases}, \quad SR < \Gamma_{Coupling} \tag{35}$$

$$T_p = T_t = a_6{\omega_p}^2 + a_7\omega_p\omega_t + a_8{\omega_t}^2, \quad SR \geq \Gamma_{Coupling} \tag{36}$$

Where $\Gamma_{Coupling}$ is the initial value of SR so that $TR = 1$.

As already explained, an ordinary least squares analysis has been performed in order to find unknown variables a_0 up to a_8.

$$AX = B$$

$$A = \begin{bmatrix} {\omega_{p,1}}^2 & \omega_{p,1}\omega_{t,1} & {\omega_{t,1}}^2 & 0 & 0 & 0 \\ 0 & 0 & 0 & {\omega_{p,1}}^2 & \omega_{p,1}\omega_{t,1} & {\omega_{t,1}}^2 \\ \dots & \dots & \dots & \dots & \dots & \dots \\ {\omega_{p,n}}^2 & \omega_{p,n}\omega_{t,n} & {\omega_{t,n}}^2 & 0 & 0 & 0 \\ 0 & 0 & 0 & {\omega_{p,n}}^2 & \omega_{p,n}\omega_{t,n} & {\omega_{t,n}}^2 \end{bmatrix} \tag{37}$$

$$B = \begin{bmatrix} T_{p,1} \\ T_{t,1} \\ \dots \\ T_{p,n} \\ T_{t,n} \end{bmatrix}, X = \begin{bmatrix} a_0 \\ a_1 \\ a_2 \\ a_3 \\ a_4 \\ a_5 \end{bmatrix} \tag{38}$$

when $SR < \Gamma_{Coupling}$.

While:

$$A = \begin{bmatrix} {\omega_{p,1}}^2 & \omega_{p,1}\omega_{t,1} & {\omega_{t,1}}^2 \\ \dots & \dots & \dots \\ {\omega_{p,n}}^2 & \omega_{p,n}\omega_{t,n} & {\omega_{t,n}}^2 \end{bmatrix}, B = \begin{bmatrix} T_{p,1} \\ \dots \\ T_{p,n} \end{bmatrix}, X = \begin{bmatrix} a_6 \\ a_7 \\ a_8 \end{bmatrix} \tag{39}$$

when $SR \geq \Gamma_{Coupling}$.

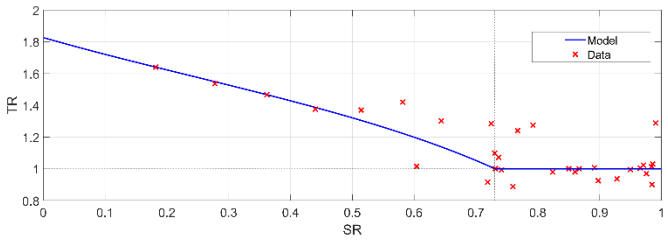

Figure 18: Torque ratio vs Speed ratio: model (blue) and experimental data (red)

Hence, once these 9 parameters have been identified from experimental data, pump and turbine torque can be computed by using eq. 35-36, while speed ratio and torque ratio through eq. 33-34.

The Figure 18 illustrates the torque ratio versus speed ratio map obtained from the model compared with experimental data points close to stationary conditions. It has been found a value $R^2 = 0.81$.

On the other side, the capacity factor model is then calculated as a ratio between the pump speed and the square root of the pump torque, in open lock-up clutch conditions; Figure 19 shows the capacity factor model output in comparison with the experimental data gathered during the acceleration tests. The ratio has been calculated from experimental data as follows:

$$CF = \frac{\omega_p}{\sqrt{T_p}} \tag{40}$$

Where CF is the capacity factor, ω_p the rotational speed of the pump, which is equal to the electric motor speed ω_{EM}, T_p and T_{EM} are the pump and EM torque respectively.

The results of the parameter estimation are reported in Figure 19. The computed R^2 value is 0.89 for the converter mode.

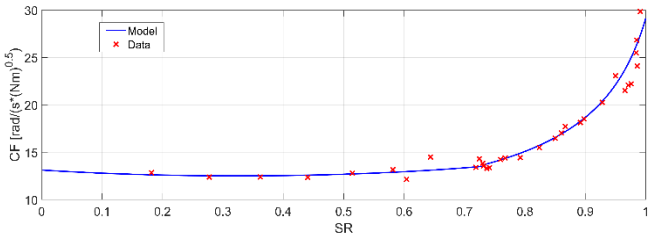

Figure 19: Torque Converter capacity factor model (blue) and measured data (red)

In the coupling mode, where SR is close to 1, the capacity factor tends to infinity if SR tends to one [35]. In this case, the model estimation has a R^2 value of around 0.75.

Gear shift thresholds

With the aim of identifying the gear shift thresholds, it is important to investigate the boundary conditions, such as speed, pedal position and torque that characterize the shifting events. To this purpose, some acceleration and deceleration tests at constant pedal position are performed. For a better understanding, Figure 20 illustrates some of the acceleration maneuvers carried out from stand-still up to 130 km/h, on the chassis dyno. As can be noticed from the bottom plot, each acceleration is performed with different steps of pedal position. In the meanwhile, the EM and the ICE rev-up and the gears are automatically shifted, as illustrated in the upper plot.

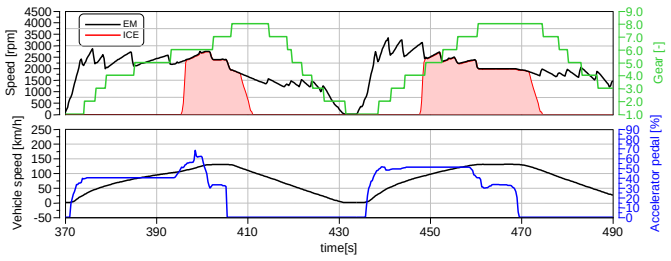

Figure 20: Acceleration test at different pedal position for gear shift thresholds identification

In this analysis, the information about vehicle speed and pedal position are recorded whenever a gearshift input command was read from the CAN; afterwards, all the shifting events are filtered out from the experimental data in order to define the gear shift thresholds, as shown in the Figure 21. Usually, on the CAN-bus network the actual gear signal can be found, which is different in time from the target one. Indeed, there is a time delay between the gearshift request and its actuation, which can cause error in the assessment of the desired thresholds. Hence, the authors used the target gear signals available form CAN. As a result, Figure 21 shows the experimental points

recorded during a shifting event, as a function of speed and accelerator pedal position. The analysis was carried out for the shifting events from the 1st up to 5th gear. Later, a linear regression was applied to obtain the gear shift threshold as is illustrated in the picture.

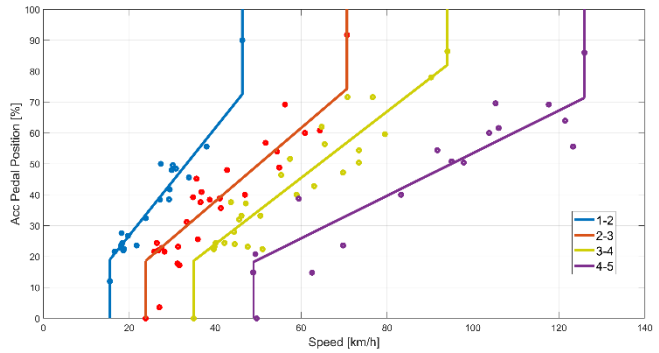

Figure 21: Gear shift thresholds modelled (colored lines) and its experimental values (dots) at different accelerator pedal position and vehicle speed

Braking system

The last part of this investigation deals with the vehicle braking system, which mixes the conventional hydraulic braking effect with the additional one provided by the electric motor/generator.

Prior to vehicle testing, it was necessary to correlate the pressure signal to the torque applied on each axle. To this purpose, braking maneuvers in neutral position (i.e. no drag/regenerative torque from the powertrain) were carried out to perform the correlation. Figure 22 illustrates the linear relationship that was found between pressure and hydraulic torque, both on the front (green) and rear (blue) axle; the equations are also reported. Results of the braking investigation will be later reported: the hydraulic braking torque is calculated by directly multiplying pressure values with the calculated coefficients, while the so-called powertrain torque at the rear wheels is calculated as the difference between rear braking torque measured by the chassis dyno and the rear hydraulic torque, since this is a Rear-Wheel-Drive vehicle (RWD).

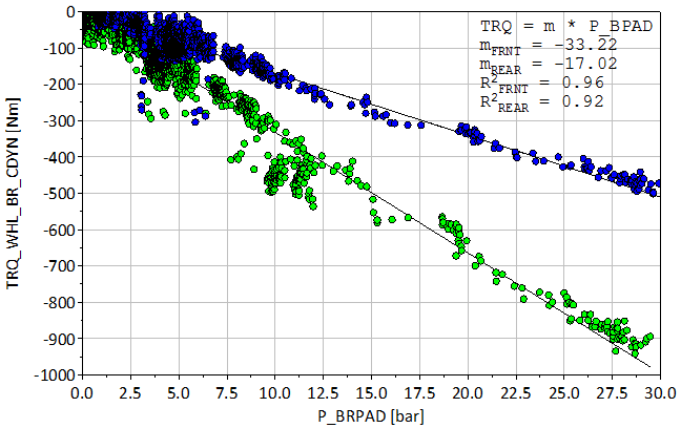

Figure 22: Rear (blue) and Front (green) Pressure - Torque correlation

Considering the linear regression performed to find the relation between the braking torque and the calipers pressure, it is possible to define a brake torque static ratio with the following equations:

$$\begin{cases} k_f = \frac{m_f}{m_f+m_r} \cdot 100 = 66\ \% \\ k_r = \frac{m_r}{m_f+m_r} \cdot 100 = 34\ \% \end{cases} \quad (41)$$

Where k_f and k_r are respectively the front and rear brake torque distribution, while m_f and m_r are respectively the front and rear gains between the hydraulic pressure and the torque on each axle.

The braking system behaviour and its effect on the vehicle dyamics were investigated over two different type of manuevers: the WLTC standard driving cycle and a series of imposed deceleration, with different level of intensity. As illustrated in Figure 23, the main signals recorded are the braking energy from the electric motor (red) and the hydraulic braking enegy, on the rear (blue) and front (green) axle. Moreover, the accelerator pedal is shown togheter with the vehicle speed and deceleration. As one can notice, the multiple deceleration test (bottom plot) was performed with a gradual but constant increase of the deceleration rate. In this type of analysis, the vehicle working points are analyzed in terms of speed and acceleration, as depicted in the bottom plot of Figure 23. In this picture, the whole set of braking points studied along the WLTC cycle (blue) and the deceleration specific test (red) is reported; it is clear how the standard driving cycle explores low level of decelerations (up to -1.8 m/s^2), while on the deceleration test more aggressive braking maneuvers were performed (up to -2.6 m/s^2).

In this regard, Figure 24 contains a group of picture useful to perform a thorough analysis of the braking system behavior: the three contours maps show values of different braking power ratios as function of vehicle acceleration and speed, while the bottom-right plot is a 2D illustration of measured braking forces. More in details, in the top-left map of Figure 24, the powertrain regenerative (only rear) braking impact over the total braking power, i.e. powertrain and hydraulic, is analyzed. It can be noticed that the powertrain contribution is relevant in the driving cycle area where low deceleration is taken into account.

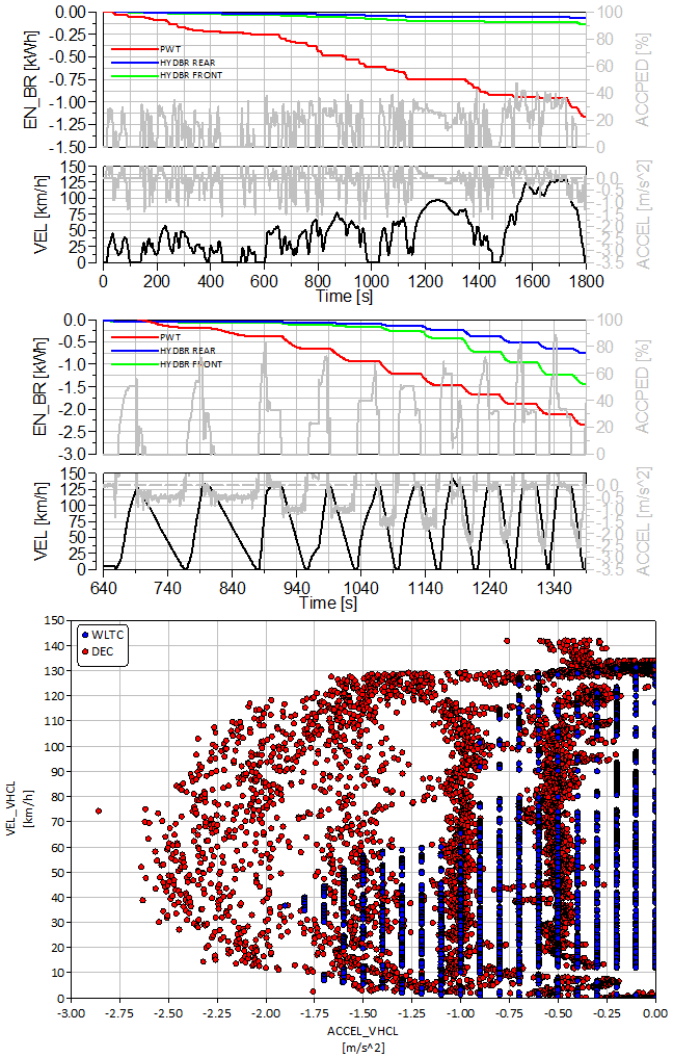

Figure 23: Main output of WLTC (top) and deceleration (center) test recorded for braking system characterization, with the explored braking points (bottom) over the WLTC (blue) and the deceleration (red) test

In this region the powertrain contributes for almost 80 to 90% to the total braking request. On the other side, in the high deceleration regions, the regenerative braking torque provides a smaller contribution, but almost constant as noticed throughout the test campaign. Furthermore, in the bottom-left map of Figure 24, the total hydraulic (front and rear) power is compared to the total braking power, showing that the total hydraulic torque linearly increases with deceleration up to the 70% of the total braking request. One can notice that at low speed (<10 km/h) the main braking contribution is provided by the hydraulic system (>90%). Finally, on the right side of Figure 24 the analysis between front and rear braking is provided: generally it can be seen that the front hydraulic brake contribution increases at high decelerations, especially in the range between -1.25 and -2 m/s^2, where vehicle stability is privileged with respect to regeneration. Moreover, as already seen, at very low speed the braking torque is provide by the hydraulic system. As for the braking force analysis, from the bottom-right plot it can be highlighted that the rear contribution is higher than the front one, especially when higher braking forces are demanded (above -1500 Nm).

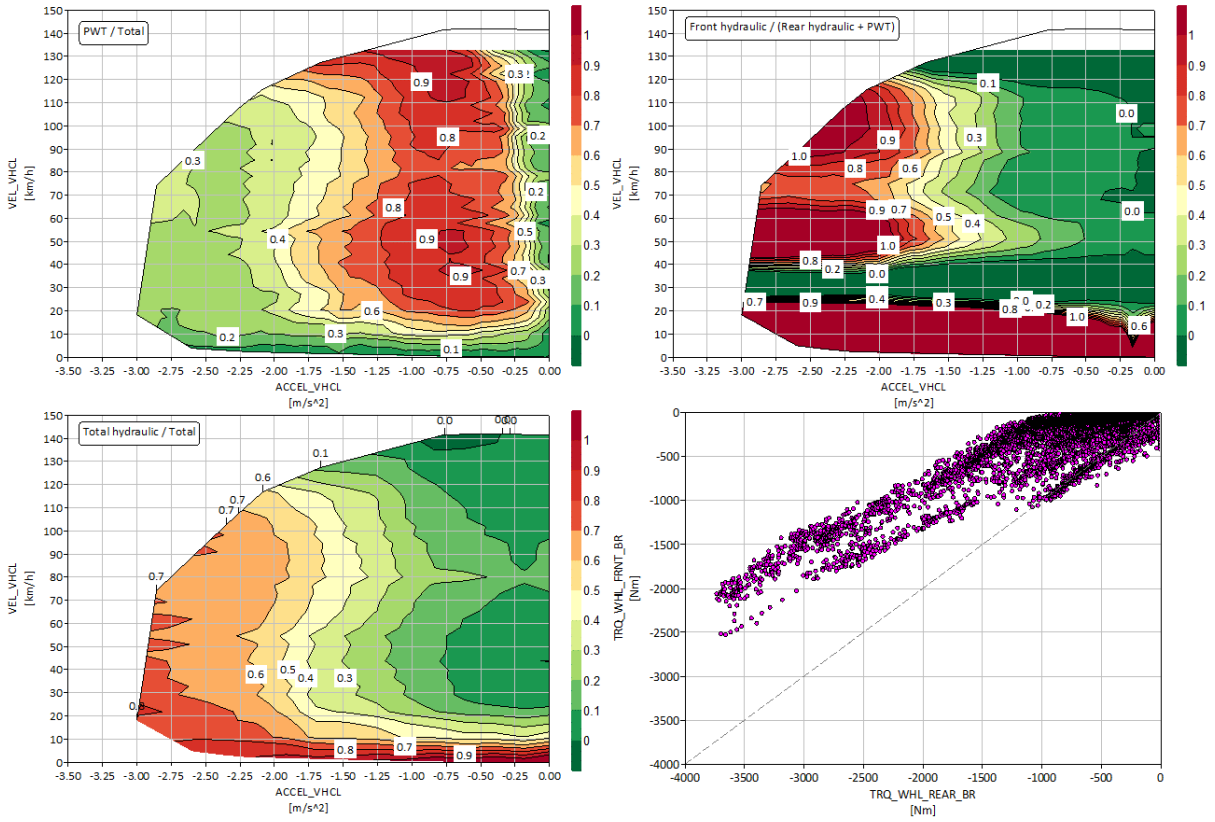

Figure 24: Vehicle brake blending analysis: regenerative (PWT) over total braking power (top-left), total hydraulic over total braking power (bottom-left), front over rear total power (top-right) and front versus rear braking force (bottom-right)

Conclusions

The presented activity illustrates the outcome of a reverse-engineering method applied on a state-of-the-art P2 Diesel Plug-In Hybrid Electric Vehicle (PHEV) equipped with AT. The dedicated instrumentation carried out on the whole powertrain is designed to be performed at vehicle level, without the need of tearing down the complete powertrain. In this framework, the main sub-system that are involved in propelling the vehicle, such as the HV and LV network, the main cooling systems used to control the powertrain thermal-management, the transmission output shaft and the braking system were instrumented. After the instrumentation phase, the case study underwent a series of dedicated but limited maneuvers that were designed a-priori in order to fully exploit the powertrain operating points. The test protocol described in this research activity involves the so-called Ramp-Up test, constant driving test for battery charging and discharging, accelerations, decelerations and the WLTC standard driving cycle. The whole experimental campaign was designed to gain a sufficient amount of data and identify the parameters that better represent the physical behavior of the main components; in order to create a consistent database and a valuable starting point for powertrain modelling.

In particular, for each subsystem under investigation, a suited testing procedure was defined with a specific target. Afterwards, the outcome of the experimental tests were processed and the parameters used to describe the components behavior (i.e. efficiency maps, BSFC, battery parameters, etc.) were identified by adopting a least mean square method. As a final step, the results of the identification process were computed and plotted together with the experimental data acquired during the testing campaign, with an indication of the coefficient of determination R^2.

As a result, the identification process showed satisfactory outcomes, especially considering the fact that the reverse-engineering methodology is performed at vehicle level. The creation of efficiency maps for the transmission, the EM and the ICE, constitutes a valuable dataset that can be later insert into a map-based vehicle model for generic assessment of vehicle potentialities. Moreover, the methodology is able to map the equivalent values of both the OCV and battery internal resistance, for the complete battery pack. Furthermore, the gearshift threshold have been found for gears from the 1st to 5th; unfortunately, the other gears could not be analyzed. Finally, with the aid of a simple instrumentation on the braking system, the main characteristic of the vehicle behavior during deceleration phases have been found, resulting in a higher regenerative contribution in the driving cycle area, while the hydraulic system mainly works at high deceleration rate or at very low vehicle speed.

As for the future, this methodology could be applied to model the engine-out and tail-pipe emission from the ICE, as well as the performance of the after-treatment system. The outcome of the complete experimental campaign and the parameter identification process can be tested with the adoption of a map-based vehicle model. Moreover, this methodology might be also applied to different hybrid architecture, in order to improve both the testing and modeling techniques. As far as this work is considered, it designs a valid reverse-engineering methodology applicable to the whole hybrid powertrain system and creates useful inputs for vehicle benchmarking and vehicle simulation.

References

1. Live-Counter.com, “How Many Cars are There in the World?,” https://www.live-counter.com/number-of-cars/, doi:https://www.carsguide.com.au/car-advice/how-many-cars-are-there-in-the-world-70629.

2. Moultak, M., Lutsey, N., and Hall, D., “Transitioning to zero-emission heavy-duty freight vehicles,” *Int. Counc. Clean Transp.* (September), 2017.

3. Johnson, T. and Joshi, A., “Review of Vehicle Engine Efficiency and Emissions,” *SAE Tech. Pap.* 2017–March(March), 2017, doi:10.4271/2017-01-0907.

4. ICCT, “European Vehicle Market Statistics - Pocketbook 2018/19,” 64, 2018.

5. Galvagno, E., Velardocchia, M., and Vigliani, A., “Drivability enhancement and transient emission reduction for a mild hybrid diesel-electric truck,” *Int. J. Powertrains* 2(2/3):262, 2013, doi:10.1504/ijpt.2013.054154.

6. Galvagno, E., Rondinelli, E., and Velardocchia, M., “Electro-Mechanical Transmission modelling for series-hybrid tracked tanks,” *Int. J. Heavy Veh. Syst.* 19(3):256–280, 2012, doi:10.1504/IJHVS.2012.047916.

7. Galvagno, E., Vigliani, A., and Velardocchia, M., “Transient response and frequency domain analysis of an electrically variable transmission,” *Adv. Mech. Eng.* 10(5), 2018, doi:10.1177/1687814018776182.

8. Galvagno, E., Morina, D., Sorniotti, A., and Velardocchia, M., “Drivability analysis of through-the-road-parallel hybrid vehicles,” *Meccanica* 48(2):351–366, 2013, doi:10.1007/s11012-012-9606-6.

9. Tinelli, V., Galvagno, E., and Velardocchia, M., “Dynamic Analysis and Control of a Dual Mode Electrically Variable Transmission,” *Mech. Mach. Sci.* 73:3731–3740, 2019, doi:10.1007/978-3-030-20131-9_368.

10. Axsen, J. and Kurani, K.S., “Hybrid, plug-in hybrid, or electric-What do car buyers want?,” *Energy Policy* 61:532–543, 2013, doi:10.1016/j.enpol.2013.05.122.

11. Senecal, P.K. and Leach, F., “Diversity in transportation: Why a mix of propulsion technologies is the way forward for the future fleet,” *Results Eng.* 4, 2019, doi:10.1016/j.rineng.2019.100060.

12. Hui, Z., Dongpu, C., and Haiping, D., “Modeling, Dynamics and Control of Electrified Vehicles,” ISBN 978-0-12-812786-5, 2018, doi:10.1016/C2016-0-03862-7.

13. Zanelli, A., “Real Time Energy Management Control Strategies for an Electrically Supercharged Gasoline Hybrid Vehicle.”

14. Zanelli, A., Millo, F., and Barbolini, M., “Driving Cycle and Elasticity Manoeuvres Simulation of a Small SUV Featuring an Electrically Boosted 1.0 L Gasoline Engine,” *SAE Tech. Pap.* 1–16, 2019, doi:10.4271/2019-24-0070.

15. Kelly, J., Scanes, P., and Bloore, P., “Specification and design of a switched reluctance 48 v belt integrated starter generator (B-ISG) for mild hybrid passenger car applications,” *SAE Tech. Pap.* 1, 2014, doi:10.4271/2014-01-1890.

16. Vallur, A.R., Khairate, Y., and Awate, C., “Prescriptive Modeling , Simulation and Performance Analysis of Mild Hybrid Vehicle and Component Optimization Mild Hybrid System- Improvement of Fuel,” *SAE Int.*, 2015, doi:10.4271/2015-26-0010.Copyright.

17. Barel, G. Van, Huybrechts, T., Vanommeslaeghe, Y., Blontrock, D., and Hellinckx, P., “Automatic Reverse Engineering of CAN BusData Using Machine Learning Techniques,” 2017, doi:10.1007/978-3-319-69835-9_71.

18. Dipierro, G., Millo, F., Scassa, M., and Perazzo, A., “An Integrated Methodology for 0D Map-Based Powertrain Modelling Applied to a 48 V Mild-Hybrid Diesel Passenger Car,” *SAE Tech. Pap.* 1–15, 2018, doi:10.4271/2018-01-1659.

19. Dipierro, G., Tansini, A., Fontaras, G., and Commission, E., “An Integrated Experimental and Numerical Methodology for Plug-In Hybrid Electric Vehicle 0D Modelling,” *SAE Tech. Pap.*, 2019, doi:10.4271/2019-24-0072.Abstract.

20. Horiba, “QUOTATION - Chassis Dynamometer VULCAN,” 2019.

21. Isabellenhütte Heusler GmbH & Co., “ISAscale® // High precision measurement,” 2015.

22. Council of the European Union, “DIRECTIVE 98/70/EC OF THE EUROPEAN PARLIAMENT AND OF THE COUNCIL of 13 October 1998 relating,” *Off. J. Eur. Communities* (350):58–67, 1998.

23. RS Components, “IEC Mineral Insulated Thermocouple with Miniature Type K Thermocouple Plug.”

24. S.r.l., A.R., “PIEZORESISTIVE PRESSION TRANSDUCER SPxx-M10x1,” 2019.

25. United Nations, Addendum 15 : Global technical regulation No . 15 - Worldwide harmonized Light vehicles Test Procedure, *Glob. Regist.* ECE/TRANS/:1–234, 2014.

26. UNECE, Regulation No. 101 Uniform provisions concerning the approval of passenger cars powered by an internal combustion engine only, or powered by a hybrid electric power train with regard to the measurement of the emission of carbon dioxide and fuel consumptio, 2013.

27. Zhang, W. and Guo, X., “Analysis and modeling of transmission efficiency of vehicle driveline,” *SAE Tech. Pap.* 1, 2014, doi:10.4271/2014-01-1779.

28. Rizzoni, G., Guzzella, L., and Baumann, B.M., “Unified

modeling of hybrid electric vehicle drivetrains," *IEEE/ASME Trans. Mechatronics* 4(3):246–257, 1999, doi:10.1109/3516.789683.

29. Heywood, J.B., "Internal combustion engine fundamentals," ISBN 9781260116106, 1988.

30. Ferrari, G., "Internal combustion engines," ISBN 9788874887651, 2014.

31. He, H., Xiong, R., and Fan, J., "Evaluation of lithium-ion battery equivalent circuit models for state of charge estimation by an experimental approach," *Energies* 4(4):582–598, 2011, doi:10.3390/en4040582.

32. Samad, N.A., Siegel, J.B., and Stefanopoulou, A.G., "Parameterization and validation of a distributed coupled electro-thermal model for prismatic cells," *ASME 2014 Dyn. Syst. Control Conf. DSCC 2014* 2, 2014, doi:10.1115/DSCC2014-6321.

33. Samad, N.A., Kim, Y., Siegel, J.B., and Stefanopoulou, A.G., "Influence of Battery Downsizing and SOC Operating Window on Battery Pack Performance in a Hybrid Electric Vehicle," *2015 IEEE Veh. Power Propuls. Conf. VPPC 2015 - Proc.*, 2015, doi:10.1109/VPPC.2015.7352966.

34. Pohl, B., "Transient torque converter performance, testing, simulation and reverse engineering," *SAE Tech. Pap.*, 2003, doi:10.4271/2003-01-0249.

35. Kotwicki, A.J., "Dynamic models for torque converter equipped vehicles," *SAE Tech. Pap.*, 1982, doi:10.4271/820393.

36. Hebbale, K., Maguire, J.M., Manager, G., and Smyth, G.J., "TORQUE CONVERTER MODEL : A MATRIX METHOD FOR KOTWICKI COEFFICIENTS Approved by :," 2006.

37. Yang, N., Qian, L., and Wu, D., "Lock-up control simulation of torque converter with lock-up clutch," *Proc. 2010 2nd Int. Conf. Futur. Comput. Commun. ICFCC 2010* 1, 2010, doi:10.1109/ICFCC.2010.5497784.

38. Liu, Z., Lei, Y., Zheng, H., Fu, Y., and Jiang, X., "Slip and lock up control of torque converter clutch at launching conditions and its temperature," *SAE Tech. Pap.* 2, 2013, doi:10.4271/2013-01-0357.

Contact Information

Acknowledgments

The authors wish to thanks Regione Piemonte for funding the research activity in the framework of the Settling Contract of FEV Italia in Torino. The authors would like to thank also all the research assistants and students involved in this work for the great effort.

Acronyms

AC	Alternate Current
AT	Automatic Transmission
BEV	Battery Electric Vehicle
BMEP	Brake Mean Effective Pressure
BSFC	Brake Specific Fuel Consumption
CAN	Controller Area Network
CD	Charge Depleting
CF	Capacity Factor
CS	Charge Sustaining
EM	Electric Motor
EV	Electric Vehicle
HCU	Hybrid Control Unit
HEV	Hybrid Electric Vehicle
HPCU	Hybrid Power Control Unit
HV	High Voltage
ICE	Internal Combustion Engine
LV	Low Voltage
MHEV	Mild Hybrid Electric Vehicle
NMC	Nickel-Manganese-Cobalt
OBD	On-Board Diagnostic
OCV	Open Circuit Voltage
OEM	Original Equipment Manufacturer
PHEV	Plug-in Hybrid Electric Vehicle
PMSM	Permanent Magnet Synchronous Motor
RL	Road Load
RWD	Rear-Wheel Drive
SOC	State of Charge
SR	Speed Ratio

TR	Torque Ratio
WLTC	Worldwide Harmonized Light-duty Test Cycle